AIAA AVIATION Forum
13-17 June 2016, Washington, D.C.
46th AIAA Fluid Dynamics Conference

10.2514/6.2016-3647

Interaction of an oblique shock with a transitional Mach 5.92 boundary layer

Prakash Shrestha[*], Anubhav Dwivedi[*], Nathaniel Hildebrand[*],
Joseph W. Nichols[†], Mihailo R. Jovanović[‡], and Graham V. Candler[§]
University of Minnesota, Minneapolis, MN, 55455, USA

We examine the unsteadiness generated by an oblique shock impinging on a hypersonic boundary layer. Earlier studies found that a $M = 2.15$ boundary layer undergoes a three-dimensional (3D) bifurcation to linear instability. Using the US3D compressible flow solver, we investigate whether this bifurcation remains 3D in the case of an oblique shock impinging on a laminar boundary layer with $M = 5.92$. We characterize the frequency and spanwise wavenumber selected by this bifurcation using Direct Numerical Simulation (DNS), Sparsity-Promoting Dynamic Mode Decomposition (SPDMD), and global stability analysis. DNS reveals that the hypersonic boundary layer remains laminar for an oblique shock angle of $\theta = 12^\circ$, but becomes unstable and transitions to turbulence once the shock angle increases to $\theta = 14^\circ$. In the second case, spanwise Fourier velocity spectra as well as SPDMD of the DNS data show that the flow selects a particular spanwise wavenumber and frequency. We investigate the origin of these length and time scales via global stability analysis about steady two-dimensional (2D) base flows obtained from DNS.

Nomenclature

DMD	Dynamic Mode Decomposition
$SPDMD$	Sparse Promoting Dynamic Mode Decomposition
$DPLR$	Data Parallel Line Relaxation
PSD	Power Spectral Density
DNS	Direct Numerical Simulation
FFT	Fast Fourier Transform
$SBLI$	Shock Boundary Layer Interaction
LES	Large Eddy Simulation
KEC	Kinetic Energy Consistent
PCA	Principle Component Analysis
ACE	Actively Controlled Expansion
DGM	Density Gradient Magnitude

I. Introduction

Shock Wave Boundary Layer Interactions (SBLI) have been a subject of various experimental and numerical investigations in recent years.[1] A sufficiently strong adverse pressure gradient from this interaction can cause the flow to separate, which changes the wave pattern. Note different flow phenomena can happen simultaneously. The flow field can become three-dimensional, unsteady, and even transition to turbulence. These 3D effects actively change pressure and skin friction distributions in the flow. This paper studies the 2D and 3D interaction between an oblique shock wave and a laminar boundary layer on a flat plate. Interest is mainly focused on the unsteady behavior observed in the interaction region.

[*]Graduate Research Assistant, Aerospace Engineering and Mechanics, AIAA Student Member.
[†]Assistant Professor, Aerospace Engineering and Mechanics, AIAA Member.
[‡]Associate Professor, Electrical and Computer Engineering, IEEE Senior Member.
[§]Russell J. Penrose and McKnight Presidential Professor, Aerospace Engineering and Mechanics, AIAA Fellow.

Laminar interactions have been studied previously using stability theory and numerical simulations. For a shock-induced separation bubble, Robinet[2] found a bifurcation of an initially 2D steady flow that evolved into a 3D unsteady state with increasing shock intensity. A secondary recirculation zone within the primary separation bubble, along with a spanwise velocity component, characterized the three-dimensionality of this interaction. Global stability analysis was performed to help explain the physical origin of this three-dimensionality, and an unstable global mode was found. Pagella et al.[3,4] examined the stability of hypersonic boundary layers over a compression ramp as well as with an impinging shock wave. By comparing simulations and experiments, they showed that non-parallel effects led to increased growth rates of the disturbances.

There are currently two explanations for the source of low-frequency unsteadiness in this problem. On the one hand, several studies have shown how shock motion is related to the turbulence of the incoming boundary layer. Although not directly related to low-frequency unsteadiness, Erengil and Dolling[5] conveyed in their experimental work on compression ramps at $M = 5.0$ how small-scale jittery motion of the shock is influenced by the passage of fluctuations in static quantities across it. Ünalmis and Dolling[6] proposed that low-frequency unsteadiness was affected by the thickening and thinning of the upstream turbulent boundary layer. More recently, Ganapathisubramani et al.[7] showed in their experimental studies that low-frequency shock motion is affected by long upstream low-speed and high-speed streaky structures. Using DNS, Wu and Martin[8] found a significant correlation between the motion of the separation line surrogate and fluctuations in the upstream boundary layer. This was in good agreement with what has been proposed by Ganapathisubramani et al.[7] However, the correlation was significantly lower when tested with the actual separation line. The upstream origin of low-frequency unsteadiness has been challenged by results from numerical simulations. In the Large Eddy Simulation (LES) of Touber and Sandham,[9] low-frequency oscillations were observed when no long coherent structures existed upstream. It was concluded that these structures are not necessary to promote the low-frequency behavior.

An extensive amount of work suggests the internal mechanism within the recirculation bubble is responsible for the unsteadiness. Dupont et al.[10] pointed out the coherence between wall pressure fluctuations at the foot of the shock and in the reattachment region for an oblique shock impinging on a flat plate turbulent boundary layer. This corresponds to the breathing character of the separation bubble. A simple model based on the entrainment characteristics of the shear layer as well as the mass recharge within the separation bubble has been proposed by Piponniau et al.[11] This model describes the unsteady motion of the reattachment point. An alternative mechanism for unsteadiness driven by a resonance mechanism involving the interaction of large structures with the tip of the incident shock was proposed by Pirozzoli and Grasso.[12] They suggest the interaction of such structures produce acoustic disturbances, which travel upstream to the separation point and lead to the unsteady low-frequency motion of the reflected shock. More recent studies by Touber and Sandham[9] as well as Sansica et al.[13] have pointed to the fact that there is no need for an upstream forcing to obtain the unsteady response. However, they also show that the upstream disturbances do provide a broad source of unsteady low-frequency motion. In a recent review, Clemens and Narayanaswamy[14] argue both the upstream and internal mechanism are always active independent of the strength of the interaction with the boundary layer.

Literature related to an oblique shock wave impinging on a laminar boundary layer at hypersonic speeds is relatively sparse. Not much work has been done on these strong interactions which can lead to transition. Benay et al.[15] performed a study of the SBLI in a hollow cylinder flare model at Mach 5.0. This experimental and numerical study was complimented with a local linear stability analysis of the laminar interactions. It was found that the oblique modes were the most unstable. More recently, Sandham et al.[16] carried out a numerical and experimental investigation on the oblique shock wave boundary layer interactions at Mach 6.0. They point out that the transition process is found to develop from the second or Mack mode instabilities superimposed on streamwise streaks.

In the present work, we investigate the 3D spatio-temporal dynamics of an oblique shock wave induced transition of a boundary layer at Mach 5.92. We do not consider any real gas effects and assume an adiabatic wall. A direct simulation of the interaction is presented. A time-averaged Power Spectral Density (PSD) at various streamwise locations of the resulting flow is carried out. This is used to obtain the relevant length scales of the 3D structures along the span. In addition to this, sparsity-promoting dynamic mode decomposition[17] of the pressure fluctuations at the wall is used to obtain the temporal frequency and spatial distribution of the dynamic modes[18] from the 3D flow field. We observe unsteady oblique structures in the transitioned flow. In order to gain additional insight into these oblique structures and their role in the process of transition, a global linear stability analysis with various spanwise wavenumbers is carried out.

The paper is structured as follows. First, we discuss the numerical setup and calculate the 2D base flows. We then use the 2D base flows to initialize the 3D flow calculations. Two interactions are considered, one resulting from a shock angle at $\theta = 12^\circ$ (small separation) and the other from a shock angle at $\theta = 14^\circ$ (large separation). Note the 2D base flow corresponding to a large separation is shown to be transitional. Next, an analysis of the spanwise PSD and SPDMD of the 3D flow field is presented. We apply global stability analysis to an intermediate shock angle $\theta = 13^\circ$ as a test case. Finally, stability analysis is performed about $\theta = 14^\circ$ and an unstable mode is found.

II. Flow configuration

A. Numerical and physical modeling

We solve the compressible Navier-Stokes equations for a perfect gas in conservative form

$$\frac{\partial U}{\partial t} + \frac{\partial F_j}{\partial x_j} = \frac{\partial F_j^{\mathrm{v}}}{\partial x_j}, \tag{1}$$

where the vector of conserved variables U is

$$U = \begin{bmatrix} \rho \\ \rho u_i \\ E \end{bmatrix} \tag{2}$$

and the convective F_j and viscous F_j^{v} fluxes are expressed as

$$F_j = \begin{bmatrix} \rho u_j \\ \rho u_i u_j + p\delta_{ij} \\ (E+p)u_j \end{bmatrix}, \qquad F_j^{\mathrm{v}} = \begin{bmatrix} 0 \\ \sigma_{ij} \\ \sigma_{ij} u_i - q_{ij} \end{bmatrix}. \tag{3a,b}$$

The fluid density ρ and temperature T are related to pressure p through the equation of state for an ideal gas given by $p = \rho RT$. In the above equations, u_i is the i^{th} component of velocity and $E = \rho c_v T + \rho u_i u_i/2$ is the total energy. The viscous flux tensor σ_{ij} is defined as $\sigma_{ij} = 2\mu S_{ij} - 2\mu S_{kk}\delta ij/3$, where S_{ij} is the symmetric part of the velocity gradient tensor. We use Fourier's law to calculate the heat flux vector q_j. Molecular viscosity μ is calculated using Sutherland's law: $\mu = aT^{1.5}/(T+b)$ with $a = 1.458 \times 10^{-6}$ and $b = 110.4$. Finally, the thermal conductivity $k = \mu c_p/Pr$ is computed with a constant Prandtl number $Pr = 0.72$ and ratio of specific heats $\gamma = 1.4$.

For the inviscid flux calculation, we implement a stable low-dissipation scheme based on the Kinetic Energy Consistent (KEC) method developed by Subbareddy and Candler.[19] In this method, the inviscid flux is split into a symmetric (nondissipative) and an upwind (dissipative) portion. The flux is pre-multiplied by a shock-detecting switch, ensuring that the dissipation occurs only around shocks.[20] We use a fourth-order central KEC scheme for the present study. Note the viscous fluxes are modeled with second-order central differences. Here time integration is performed using an implicit second-order Euler method with point relaxation to maintain numerical stability and accuracy. The implicit system is also solved with the full matrix Data Parallel Line Relaxation (DPLR) method, which has good parallel efficiency.[21]

B. Calculation of 2D base flows

We consider a laminar boundary layer for this base flow at $M_\infty = 5.92$ with a unit Reynolds number equal to 4.6×10^6 m^{-1}. The freestream temperature and pressure are $T_\infty = 53.06$ K and $p_\infty = 308.2$ Pa, respectively. These conditions match the experiments performed in the ACE Hypersonic Wind Tunnel[22] at Texas A&M University. Note the computational domain used for this base flow is shown in Figure 1. Here X_{sep} denotes the separation length and X_{sh} is the interaction length. The inflow conditions for simulating the SBLI are obtained separately. A computation of zero pressure gradient boundary layer flow over a flat plate with a round leading edge ($r = 10^{-4}$ m) was carried out (see Appendix). The flow profile obtained at $x = 40$ mm from the leading edge is shown in Figure 2. Here the Reynolds number based on the displacement thickness at the inflow is 2.242×10^3. An oblique shock wave is made by imposing the Rankine-Hugoniot conditions. The oblique shock is generated such that the inviscid shock impinges at a fixed distance of 0.25 meters from

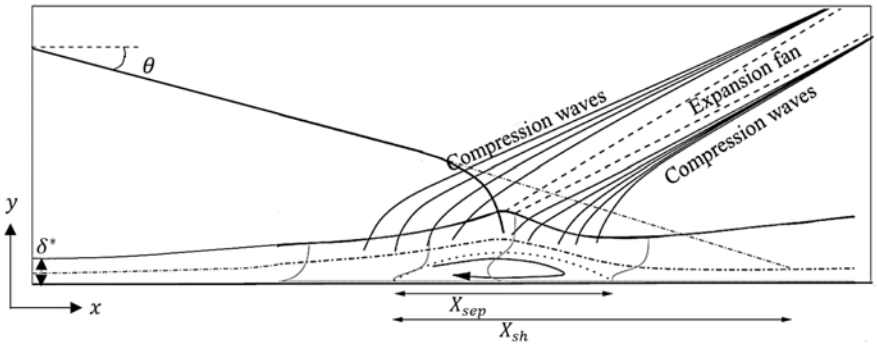

Figure 1: A sketch of the domain for the 2D base flows.

the inflow. Two base flows are computed that correspond to different strengths of the shock: $\theta = 12°$ and $\theta = 14°$. An intermediate base flow with $\theta = 13°$ was also computed for the linear stability analysis. The nondimensional length scale used in this study is the displacement thickness of the undisturbed laminar boundary layer at the inviscid impingement location. Note that the value of this displacement thickness is $\delta^* = 9.8 \times 10^{-4}$ m.

In order to accurately simulate the SBLI, a stretched grid is used in the wall normal direction with $y^+ = 0.5$. The grid points are also stretched in the streamwise direction with $x^+ = 20$. Grid clustering is done near the interaction zone to avoid large aspect ratio cells in this region. We obtain the variation of

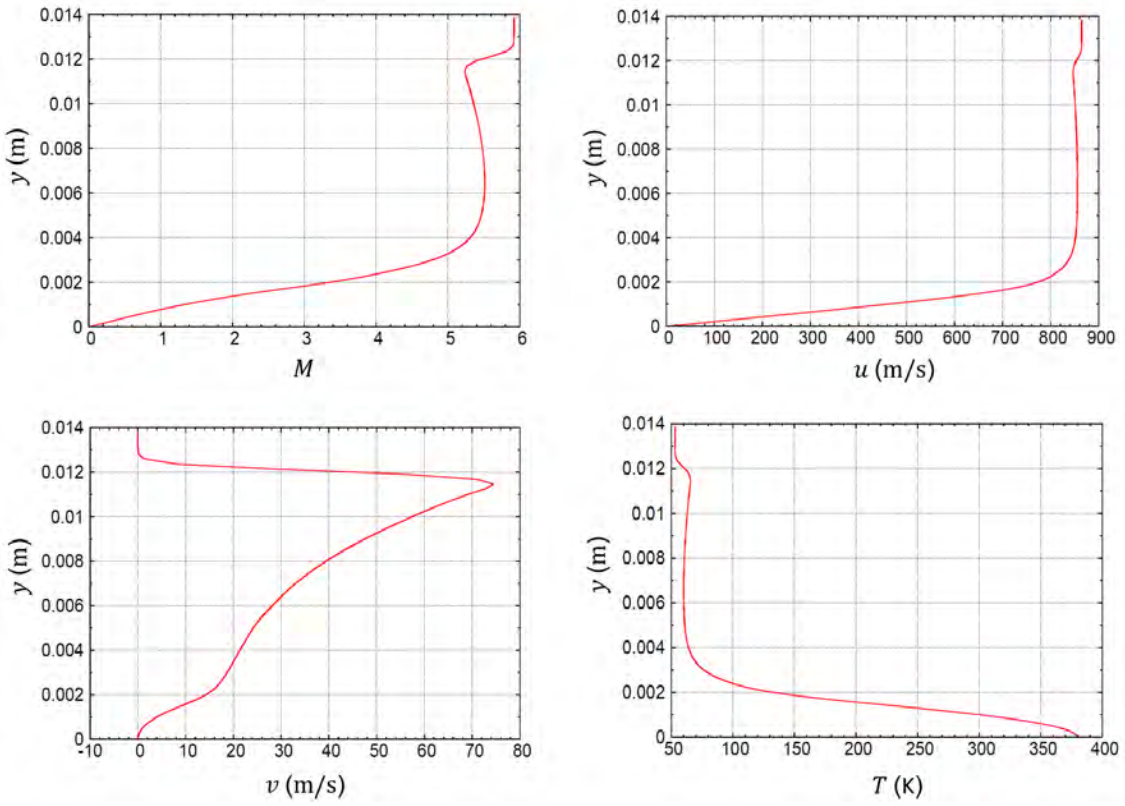

Figure 2: Plots of Mach number, streamwise velocity, cross-stream velocity, and temperature at the inlet. Note y is the distance from the wall in the cross-stream direction.

skin friction coefficient with the number of points in the streamwise n_x and cross-stream n_y directions to carry out a grid convergence study. The separation bubble is defined to exist in the zone where the wall skin friction becomes negative for the first time before switching back to positive. This is shown in Figure 3

for two oblique shock angles. Changes in the size of the bubble (nondimensionalized with δ^*) are shown in Table 1. Based on this study we choose a grid with $(n_x, n_y) = (848, 350)$ for a shock wave angle of $\theta = 12^\circ$ and $(n_x, n_y) = (998, 450)$ for $\theta = 14^\circ$.

Table 1: A grid convergence study for the 2D base flows. Here the separation bubble size in millimeters is calculated for a range of total mesh points.

$n_x \times n_y$	Bubble size for $\theta = 12^\circ$	Bubble size for $\theta = 14^\circ$
748×250	131.2 mm	295.4 mm
848×350	138.1 mm	302.0 mm
998×450	139.8 mm	310.7 mm
1098×450	140.2 mm	313.4 mm
1198×550	140.2 mm	314.0 mm
1500×550	--	314.2 mm

C. Setup of 3D simulations

The 2D base flows described in the previous section are now used as initial conditions for carrying out the 3D calculations. Here the 2D domain is extruded in the spanwise direction and periodic boundary conditions are enforced. The bottom wall is assumed to be adiabatic for the 2D and 3D base flows. We employed a supersonic outlet condition at the top and far right boundaries. In the present study, we consider three different spanwise lengths. Note the grid information for the 3D calculations is specified in Table 2. The grid is uniform in the spanwise direction with $z^+ = 100$ for all three cases. We only show results that were computed with the Grid 2 domain for brevity.

Table 2: Grid information for the 3D simulations.

Grid parameters	Grid 1	Grid 2	Grid 3
Streamwise length	500 mm	500 mm	500 mm
Wall normal length	100 mm	100 mm	100 mm
Spanwise length	100 mm	200 mm	250 mm
$n_x \times n_y \times n_z$	$998 \times 450 \times 200$	$998 \times 450 \times 400$	$998 \times 450 \times 500$

III. Results

A. 2D base flows

Different strengths of the oblique shock wave were considered for this paper. Two shock strengths corresponding to a small ($\theta = 12^\circ$) and large ($\theta = 14^\circ$) separation are presented here. This classification is defined in the work by Sansica et al.[13] The wall skin friction coefficient for both cases is shown in Figure 3. Note the small separation corresponds to the formation of a single primary recirculation zone. The large separation corresponds to the formation of a secondary bubble inside the primary recirculation zone resulting in a finite region of positive skin friction. We ran the 2D simulations for roughly 60 flow through times to obtain the steady base flows. The Reynolds number based on streamwise length at the interaction location is 1.33×10^6 for both cases. Figure 4 shows the base flow with an oblique shock angle of $\theta = 12^\circ$. The base flow corresponding to $\theta = 14^\circ$ is shown in Figure 5. We found that the base flow for $\theta = 12^\circ$ remains 2D and stable, whereas the base flow for $\theta = 14^\circ$ becomes 3D and unsteady.

B. 3D unsteady flow

In order to understand the low-frequency unsteadiness appearing in the SBLI for a large separation, we carry out 3D calculations using the 2D laminar solution with $\theta = 14^\circ$ as the initial condition. Ideally the spanwise length should be as large as possible for the 3D instabilities to appear spontaneously. The flow is allowed to

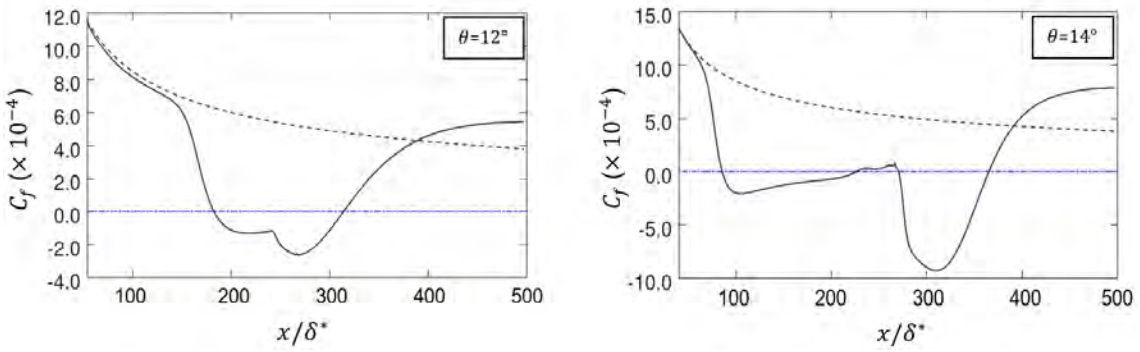

Figure 3: Skin friction coefficient distribution for the 2D base flows. Here the dotted line denotes the compressible laminar solution without an oblique shock interaction.

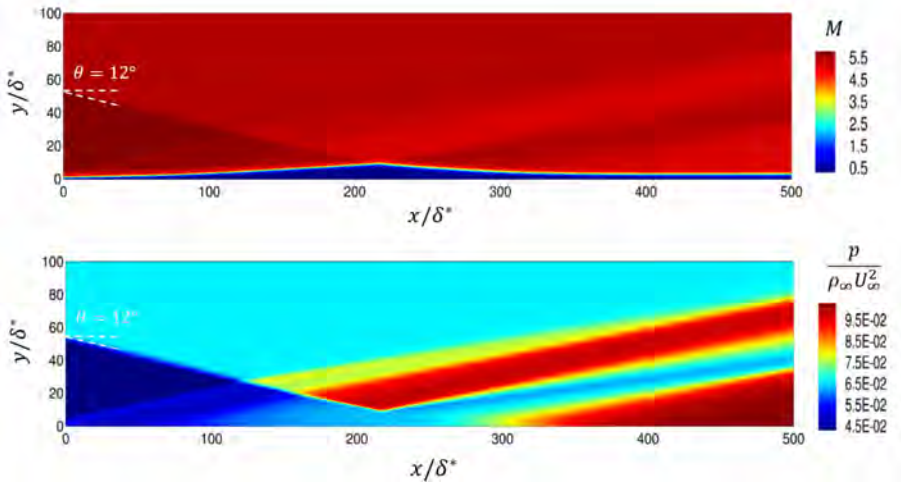

Figure 4: Contour plots of Mach number and nondimensional pressure for the base flow with an oblique shock angle of $\theta = 12°$.

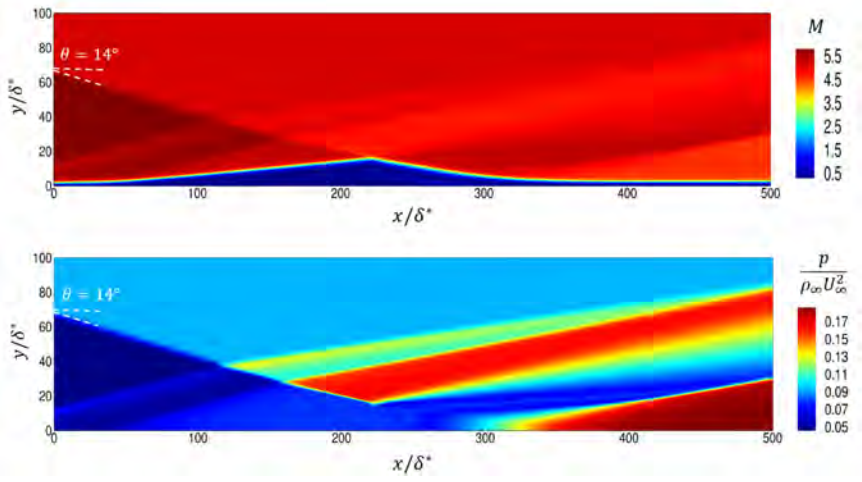

Figure 5: Contour plots of Mach number and nondimensional pressure for the base flow with an oblique shock angle of $\theta = 14°$.

develop in time. We notice that the flow field becomes fully three-dimensional inside the interaction zone as well as downstream of it after ten flow through times. This result is similar to what has been obtained by some previous studies[2] at a much lower Mach number. The shock wave angle in this case is strong enough

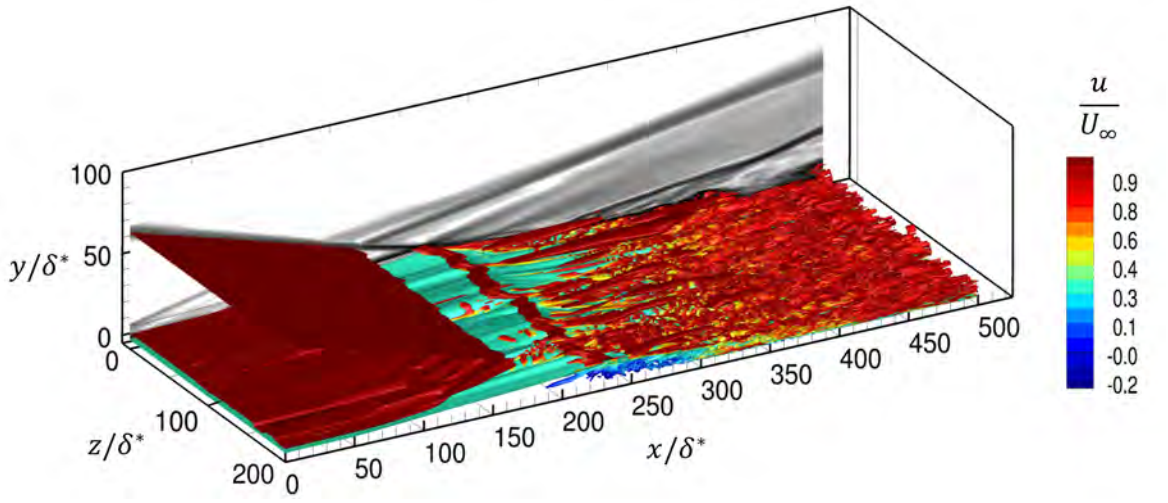

Figure 6: A snapshot of Q-criterion isosurfaces colored with nondimensional streamwise velocity. The Density Gradient Magnitude (DGM) is also shown along the xy-plane at $z = 0$.

to cause transition downstream of the reattachment point. This can be seen in Figure 6, which shows a snapshot of Q-isosurfaces colored with streamwise velocity. Figure 7 displays a snapshot of the spanwise velocity at different downstream locations. The spatial development of the 3D flow field can clearly be seen in Figures 6, 7, and 8. Notice that the flow near the separation point, and inside the boundary layer, is unsteady with a large wavelength in the spanwise direction. Small vortical structures also start to form in this region ($x \approx 100\delta^*$). These structures start merging together as we go further downstream inside

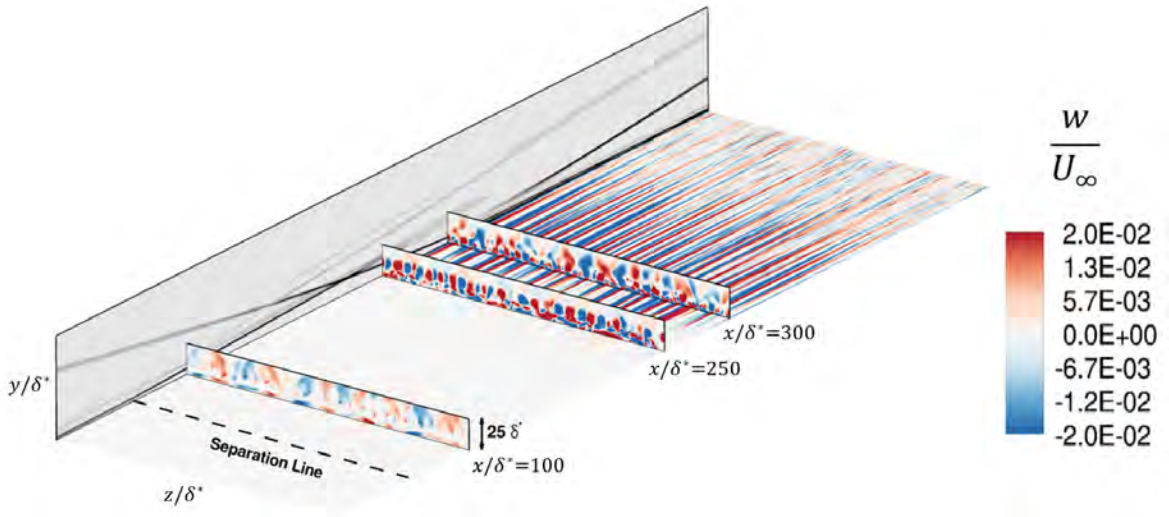

Figure 7: A snapshot of the nondimensional spanwise velocity at different downstream locations. Note the DGM is also shown along the xy-plane at $z = 0$.

the recirculation bubble ($x \approx 250\delta^*$). We see near the reattachment point that these vortical structures form streamwise streaks and eventually break apart. This is shown in Figure 8 with a snapshot of the skin friction coefficient. Close to the reattachment point ($x \approx 300\delta^*$) we notice these unsteady structures exist substantially above the wall. It is interesting to note that the transitioned flow appears to be selecting flow features with an almost constant spanwise wavelength.

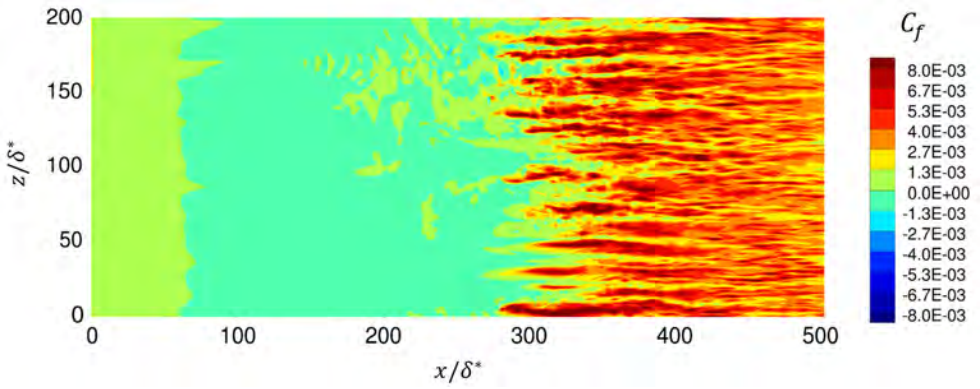

Figure 8: A snapshot of the skin friction coefficient along the bottom wall. Notice the long streamwise streaky structures.

C. Spatio-temporal analysis

Three-dimensional simulations of the transitional hypersonic boundary layer indicate that a particular spanwise length scale is selected. To further quantify this effect, we perform Fast Fourier Transforms (FFT) in the spanwise direction and average over time. Various probe locations are shown in Table 3. The spanwise velocity fluctuations are obtained at a fixed rate of 8.65×10^{-3} flow through times. We use roughly

Table 3: The location for three spanwise series of more than one hundred probes.

Direction	Probe 1	Probe 2	Probe 3
x/δ^*	100	250	300
y/δ^*	0.5	0.5	0.5

thirty samples to obtain the PSD of the spanwise velocity fluctuations that is shown in Figure 9. There are significant variations in the PSD for different nondimensional spanwise wavenumbers β. Here β has been nondimensionalized by the displacement thickness δ^*. From Figure 9, we observe a local energy maximum at $\beta = 0.18$ for the three streamwise locations. Note dominant large spanwise length scales are present

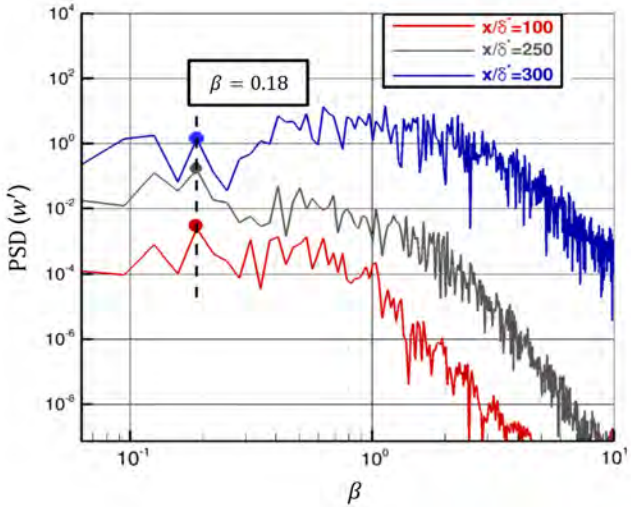

Figure 9: Plots of the PSD versus nondimensional spanwise wavenumber for three streamwise locations. Notice the local maximum at $\beta = 0.18$.

throughout the recirculation bubble. We also see that smaller scales become energetically significant downstream. In general, energy is smallest near the separation point then increases inside the bubble and after reattachment. The reason for this energy difference is that fluctuations generated inside the recirculation bubble are amplified as they travel downstream.

In addition to the spanwise FFT analysis, we perform SPDMD[17] to study the temporal contents of the flow field. Dynamic Mode Decomposition (DMD) is an effective means for capturing the essential features of numerically or experimentally generated flow fields. We use SPDMD because it achieves desirable tradeoff between the number of dynamic modes and quality of approximation.[17] Both stability tools were applied

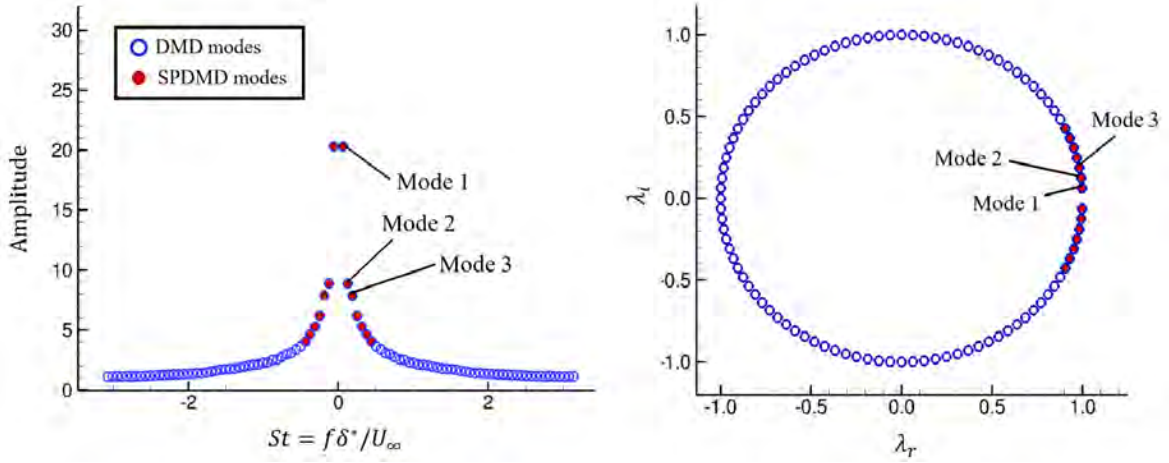

Figure 10: Plot of the amplitude versus frequency and an eigenvalue spectrum calculated from DMD and SPDMD for $\theta = 14°$.

along the bottom wall. Approximately one hundred snapshots of the wall pressure fluctuations were used for each method. We found the two most dominant modes had frequencies of $St = 0.002$ and $St = 0.005$, respectively. In Figure 10, an eigenvalue spectrum and plot of the amplitude versus frequency computed from DMD and SPDMD are shown. We plot the two most dominant modes with contours of the pressure fluctuations in Figure 11. Notice the presence of several streak like structures downstream of the interaction region. These SPDMD results are preliminary and a more in depth study needs to be done.

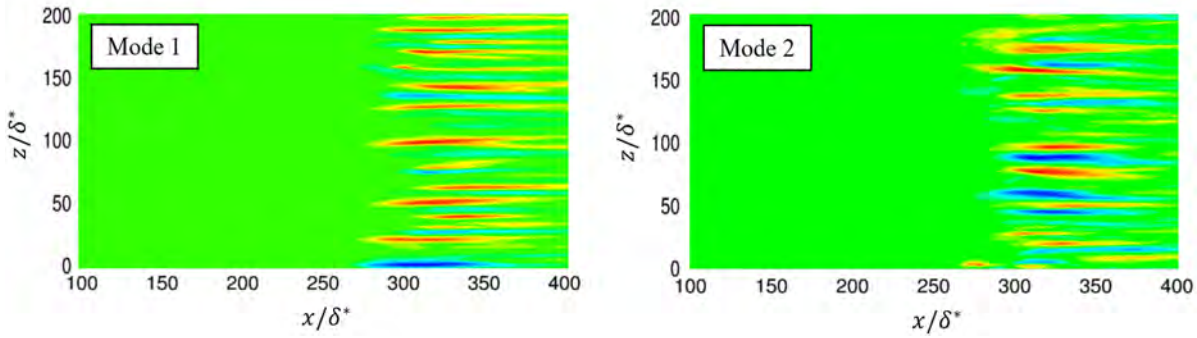

Figure 11: Contour plots of the pressure fluctuations along the wall for the two most dominant SPDMD modes. Here red denotes a positive pressure while blue is negative.

D. Global stability analysis

Linear stability theory is used to gain more information about these streamwise streaks and their role in the process of transition. In the following stability analysis, we consider the behavior of small perturbations about a steady base flow. The perturbation dynamics are governed by the 2D Linearized Navier-Stokes (LNS) equations.[23] We nondimensionalize these equations with respect to the freestream velocity, temperature,

and density at the inlet denoted by U_∞, T_∞, and ρ_∞, respectively. Note the boundary layer displacement thickness δ^* was also used in this nondimensionalization.[24] The LNS equations were discretized by fourth-order centered finite differences applied on a stretched mesh. This resulted in a large sparse matrix.[25] For the impulse simulations, the equations were advanced in time with an explicit fourth-order Runge-Kutta scheme. Global modes were extracted by the shift-and-invert Arnoldi method as implemented by the software package ARPACK.[26] The inversion step was computed by finding the LU decomposition of the shifted sparse matrix using the massively parallel SuperLU package.[27] Finally, numerical sponge layers were employed at the top, left, and right boundaries to absorb outgoing acoustic waves.

We begin global stability analysis of the hypersonic oblique shock wave/laminar boundary layer interaction by first considering its response to a localized pressure impulse for $\theta = 12°$. The resulting wavepacket illustrates the different spatio-temporal dynamics of the linearized system. It also provides physical insight useful to the interpretation of the global modes discussed in the next paragraph. A comparison between

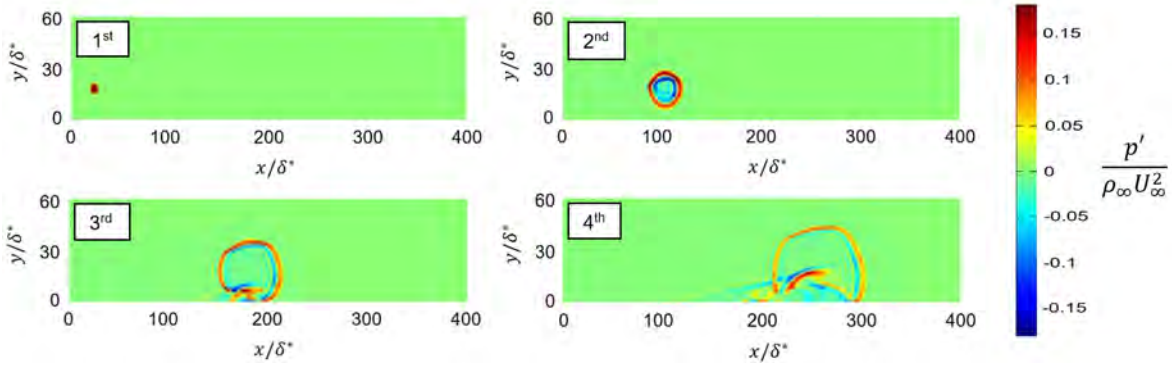

Figure 12: Linear response of the SBLI to an initial pressure disturbance for $\theta = 12°$.

the linear and nonlinear impulse responses at early flow times resulted in good agreement. Figure 12 shows a snapshot of the wavepacket, which develops from an initial Gaussian perturbation near the inlet. Notice that the wavepacket starts to interact with the recirculation bubble as it travels downstream.

Now we consider a test case where $\theta = 13°$. This is between the previous stable and unstable cases so we expect marginal stability. We resolve 3D instabilities using a spanwise wavenumber $\beta = 2\pi/40$, which comes from Figure 9 where the flow selects a spanwise wavelength of about 40 mm in the separation zone. The Strouhal number is defined as $St = f\delta^*/U_\infty$. Figure 13 shows an eigenvalue spectrum resulting from

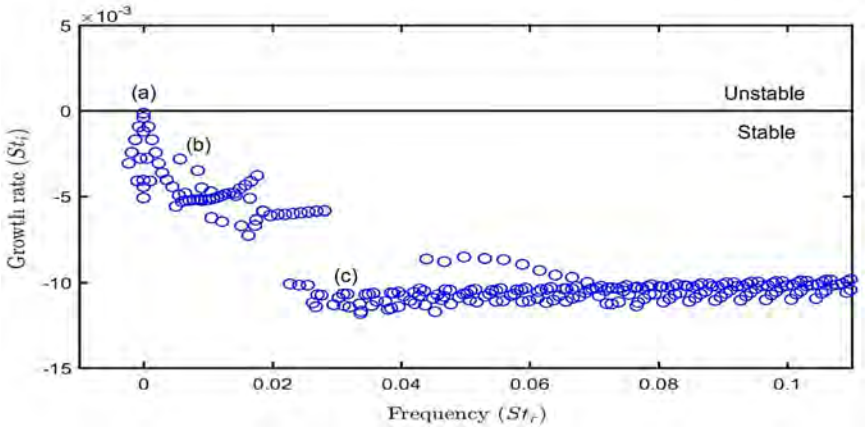

Figure 13: An eigenvalue spectrum computed from linear stability theory of the SBLI for $\theta = 13°$ and $\beta = 2\pi/40$.

the shift-and-invert Arnoldi method. The shifts were chosen along the real axis to capture the least stable modes. We spaced shifts closely together so that a portion of the spectrum converged at each shift partially overlapped with a portion converged at neighboring shifts. Twenty eigenvalues were sought at each one of

the thirty shifts. Modes corresponding to redundant eigenvalues extracted by neighboring shifts were found to agree well, providing one check on the convergence of the Arnoldi method. To further test convergence, the calculations will be repeated on a much finer mesh. The growth rate for every eigenvalue in Figure 13

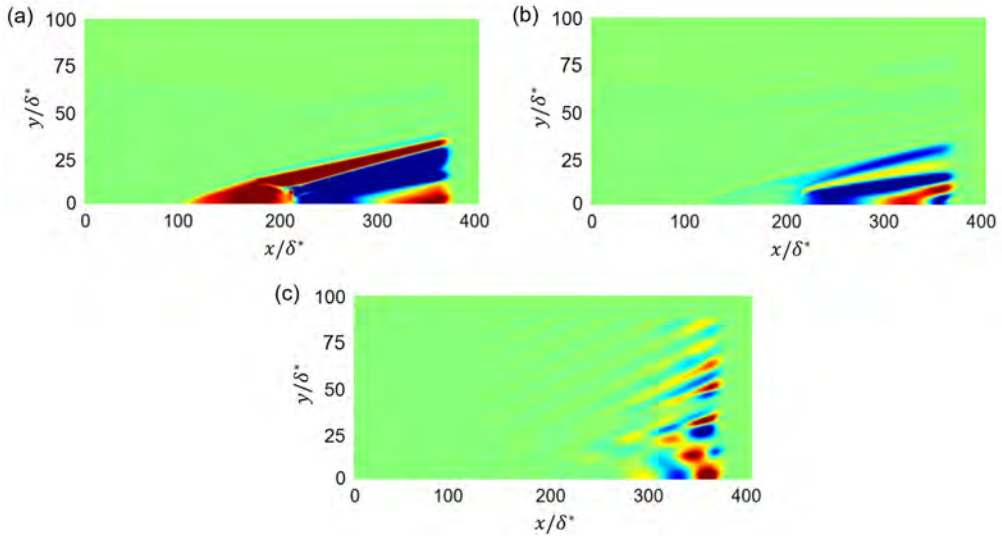

Figure 14: Global modes corresponding to labels in Figure 13 colored with the real part of the pressure perturbation. Here red denotes a positive pressure while blue is negative.

is negative; therefore, the flow is globally stable. Figure 14 shows three stable global modes visualized by contours of the real part of the pressure perturbation. We selected these eigenmodes to see if they capture the correct physics of the SBLI. From Figure 13, we observe that mode (a) encloses the recirculation bubble and extends to the right boundary where pressure gets driven to zero by the sponge layer. Mode (b) seems like it is connected to the boundary layer and reflected shock. Finally, mode (c) captures some of the acoustic radiation in the flow.

The last case we consider is a shock angle of $\theta = 14°$ where the flow becomes unsteady. We used a larger domain and stretched grid with $(n_x, n_y) = (800, 200)$. A spanwise wavenumber $\beta = \pi/10$ was found to be the most unstable. Figure 15 shows an eigenvalue spectrum resulting from the shift-and-invert Arnoldi method

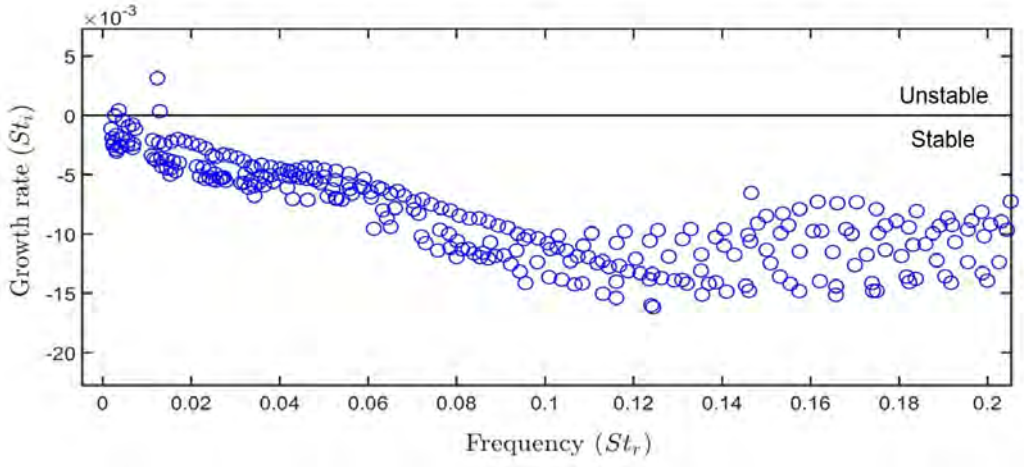

Figure 15: An eigenvalue spectrum computed from linear stability theory of the SBLI for $\theta = 14°$ and $\beta = \pi/10$.

for this case. The spectrum in Figure 15 looks more complete compared to the previous one in Figure 13. Notice that three eigenvalues have a positive growth rate; therefore, the flow is globally unstable. Figure

16 shows the most unstable global mode visualized in 3D by contours of the real part of the normalized streamwise velocity perturbation. We see that the unstable mode in Figure 16 has long streamwise streaks

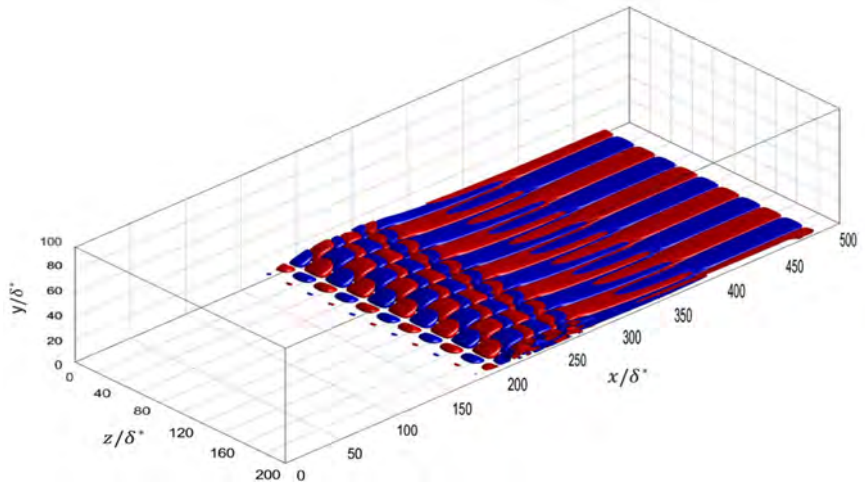

Figure 16: The most unstable mode in Figure 15 visualized by the real part of the normalized streamwise velocity perturbation. Here red denotes a positive velocity while blue is negative.

that look similar to the structures observed in Figure 8 and Figure 11. It also has a part that originates in the shear layer. The presence of these 3D unstable disturbances point to the importance of linear amplification in the interaction zone. Further analysis needs to be done in order to illustrate the role of these periodic disturbances in the development of the 3D unsteady state observed in DNS.

IV. Conclusions

Two base flow configurations corresponding to oblique shock angles of $\theta = 12^\circ$ (small separation) and $\theta = 14^\circ$ (large separation) were computed. The stability properties of these two base flows varied significantly. We saw that the 3D simulations for $\theta = 14^\circ$ became unsteady and developed long streamwise streaks after the recirculation zone. Note the case where $\theta = 12^\circ$ was steady. A spanwise FFT at different streamwise locations was carried out to obtain a spatial distribution of wavenumbers corresponding to the energetically significant structures for the case with large separation. In particular, we found that the longer wavelengths mainly contributed to the unsteadiness. Furthermore, to investigate the temporal characteristics of these streamwise structures, we applied SPDMD on the wall of the 3D flow field. Wall pressure fluctuations of the two most dominant SPDMD modes with frequencies $St = 0.002$ and $St = 0.005$ revealed long streaks. It was also found that a large amount of amplification occurs near the reattachment of the shear layer. We carried out a global stability analysis at an intermediate shock angle of $\theta = 13^\circ$ as a test case. The resulting eigenvalue spectrum was observed to be nominally stable for $\beta = 2\pi/40$. Modes corresponding to the recirculation zone, boundary layer, and acoustics were obtained. Finally, we applied linear stability analysis about $\theta = 14^\circ$ and got an unstable eigenvalue spectrum for $\beta = \pi/10$. The most unstable mode had long streamwise streaks consistent with SPDMD and the 3D simulations.

The current study illustrates the presence of long streamwise streaks. Both the spatio-temporal analysis and global stability analysis clearly point to the origin of these unsteady structures in the separated shear layer. However, a more detailed analysis of the flow field via the SPDMD needs to be performed. The low-frequency unsteadiness associated with these long streak like structures needs to be resolved over a longer period of time. It would be interesting to understand the effect of forcing on the 2D base flows considered in the present study. Forcing upstream of and inside the recirculation bubble might give more information about the receptivity of the flow to various disturbances. We could also investigate intermediate shock angles to obtain the exact point of 3D bifurcation. The effect of an isothermal wall could be analyzed. An input-output analysis[28] of this flow configuration based on the recent work by Jeun et al.[29] can also help in answering several questions related to the origins of this unsteadiness. Finally, a detailed comparison to experiments would be beneficial.

Appendix

We show the grid used for the 2D calculation of zero pressure gradient boundary layer flow without an impinging shock in Figure 17. Notice that it's stretched near the adiabatic wall with $y^+ = 0.5$. The total grid size is $(n_x, n_y) = (685, 399)$. Figure 18 shows a plot with contours of Mach number for this flow. We

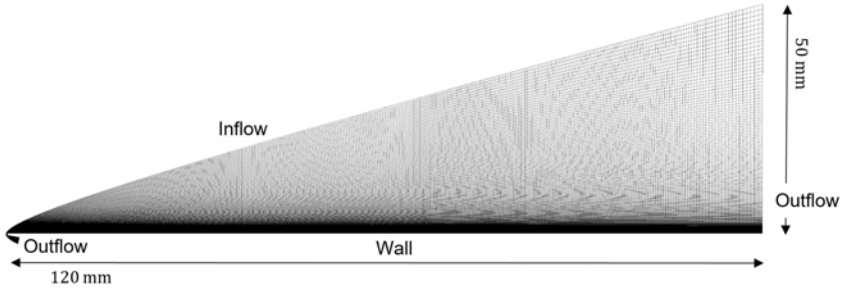

Figure 17: Stretched grid used for the 2D calculation of the incoming boundary layer.

curve the inlet so that it aligns with the bow shock. Note the dashed white line in Figure 18 represents the location where we extracted the boundary layer profiles (shown in Figure 2), which were used as the inlet condition for the 2D base flows. Here the flat plate has a leading edge radius of 0.1 mm.

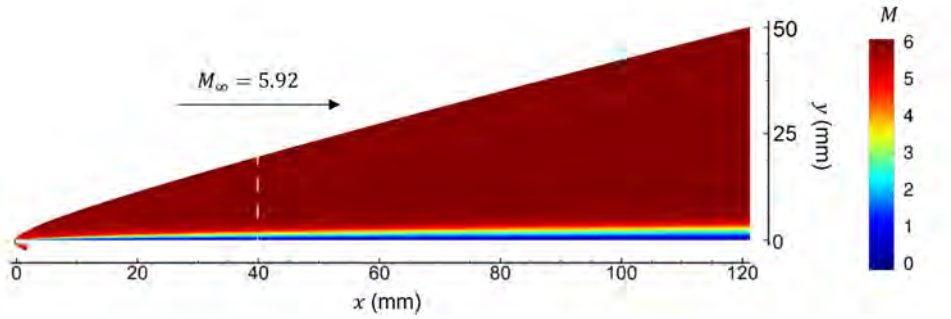

Figure 18: A plot with contours of Mach number for the 2D calculation of the incoming boundary layer. The white line represents the location where we extracted the profiles.

Acknowledgments

We are grateful to the Office of Naval Research for their support of this study through grant number N00014-15-1-2522.

References

[1]Délery, J. and Dussauge, J.-P., "Some physical aspects of shock wave/boundary layer interactions," *Shock Waves*, Vol. 19, 2009, pp. 453-468.

[2]Robinet, J.-Ch., "Bifurcations in shock-wave/laminar-boundary-layer interaction: global instability approach," *Journal of Fluid Mechanics*, Vol. 579, 2007, pp. 85-112.

[3]Pagella, A., Rist, U., and Wagner, S., "Numerical investigations of small-amplitude disturbances in a boundary layer with impinging shock wave at Ma=4.8," *Physics of Fluids*, Vol. 14, No. 7, 2002, pp. 2088-2101.

[4]Pagella, A., Babucke, A., and Rist, U., "Two-dimensional numerical investigations of small-amplitude disturbances in a boundary layer at Ma=4.8: compression corner versus impinging shock wave," *Physics of Fluids*, Vol. 16, No. 7, 2004, pp. 2272-2281.

[5]Erengil, M. E. and Dolling, D. S., "Unsteady wave structure near separation in a Mach 5 compression ramp interaction," *AIAA Journal*, Vol. 29, No. 5, 1991, pp. 728-735.

[6]Ünalmis, Ö. H. and Dolling, D. S., "Decay of wall pressure field and structure of a Mach 5 adiabatic turbulent boundary layer," AIAA Paper No. 1994-2363, June 1994, pp. 1-9.

[7]Ganapathisubramani, B., Clemens, N. T., and Dolling, D. S., "Effects of upstream boundary layer on the unsteadiness of shock-induced separation," *Journal of Fluid Mechanics*, Vol. 585, 2007, pp. 369-394.

[8]Wu, M. and Martin, M. P., "Direct numerical simulation of supersonic turbulent boundary layer over a compression ramp," *AIAA Journal*, Vol. 45, No. 4, 2007, pp. 879-889.

[9]Touber, E. and Sandham, N. D., "Large-eddy simulation of low-frequency unsteadiness in a turbulent shock-induced separation bubble," *Theoretical and Computational Fluid Dynamics*, Vol. 23, No. 2, 2009, pp. 79-107.

[10]Dupont, P., Debiève, J.-F., Dussauge, J.-P., Ardissonne, J. P., and Haddad, C., "Unsteadiness in shock wave/boundary layer interaction," Aérodynamique des Tuyères et Arrières-Corps, Technical Report, ONERA, September 2003.

[11]Piponniau, S., Dussauge, J.-P., Debiève, J.-F., and Dupont, P., "A simple model for low-frequency unsteadiness in shock-induced separation, *Journal of Fluid Mechanics*, Vol. 629, 2009, pp. 87-108.

[12]Pirozzoli, S. and Grasso, F., "Direct numerical simulation of impinging shock wave/turbulent boundary layer interaction at $M = 2.25$, *Physics of Fluids*, Vol. 18, No. 6, 2006, pp. 1-17.

[13]Sansica, A., Sandham, N. D., and Hu, Z., "Forced response of a laminar shock-induced separation bubble," *Physics of Fluids*, Vol. 26, No. 9, 2014, pp. 1-14.

[14]Clemens, N. T. and Narayanaswamy, V., "Low-frequency unsteadiness of shock wave/turbulent boundary layer interactions," *Annual Review of Fluid Mechanics*, Vol. 46, 2014, pp. 469-492.

[15]Benay, R., Chanetz, B., Mangin, B., Vandomme, L., and Perraud, J., "Shock wave/transitional boundary-layer interactions in hypersonic flow," *AIAA Journal*, Vol. 44, No. 6, 2006, pp. 1243-1254.

[16]Sandham, N. D., Schülein, E., Wagner, A., Willems, S., and Steelant, J., "Transitional shock-wave/boundary-layer interactions in hypersonic flow," *Journal of Fluid Mechanics*, Vol. 752, 2014, pp. 349-382.

[17]Jovanović, M. R., Schmid, P. J., and Nichols, J. W., "Sparsity-promoting dynamic mode decomposition," *Physics of Fluids*, Vol. 26, No. 2, 2014, pp. 1-22.

[18]Schmid, P. J., "Dynamic mode decomposition of numerical and experimental data," *Journal of Fluid Mechanics*, Vol. 656, 2010, pp. 5-28.

[19]Subbareddy, P. K. and Candler, G. V., "A fully discrete, kinetic energy consistent finite-volume scheme for compressible flows," *Journal of Computational Physics*, Vol. 228, No. 5, 2009, pp. 1347-1364.

[20]Ducros, F., Ferrand, V., Nicoud, F., Weber, C., Darracq, D., Gacherieu, C., and Poinsot, T., "Large-eddy simulation of the shock/turbulence interaction," *Journal of Computational Physics*, Vol. 152, No. 2, 1999, pp. 517-549.

[21]Wright, M. J., Candler, G. V., and Bose, D., "Data-parallel line relaxation method for the NavierStokes equations," *AIAA Journal*, Vol. 36, No. 9, 1998, pp. 1603-1609.

[22]Semper, M. T., Pruski, B. J., and Bowersox, R. D. W., "Freestream turbulence measurements in a continuously variable hypersonic wind tunnel," AIAA Paper No. 2012-0732, June 2012, pp. 1-13.

[23]Nichols, J. W., Lele, S. K., and Moin, P., "Global mode decomposition of supersonic jet noise," Center for Turbulence Research, Annual Research Briefs, Stanford University, 2009, pp. 3-15.

[24]Guiho, F., Alizard, F., and Robinet, J.-Ch., "Instabilities in oblique shock wave/laminar boundary-layer interactions," *Journal of Fluid Mechanics*, Vol. 789, 2016, pp. 1-35.

[25]Nichols, J. W. and Lele, S. K., "Global modes and transient response of a cold supersonic jet," *Journal of Fluid Mechanics*, Vol. 669, 2011, pp. 225-241.

[26]Lehoucq, R. B., Sorensen, D. C., and Yang, C., "ARPACK Users' Guide: Solution of Large-Scale Eigenvalue Problems with Implicitly Restarted Arnoldi Methods," Society for Industrial and Applied Mathematics, 1997.

[27]Li, X. S. and Demmel, J. W., "SuperLU_DIST: a scalable distributed memory sparse direct solver for unsymmetric linear systems," *ACM Transactions on Mathematical Software*, Vol. 29, No. 2, 2003, pp. 110-140.

[28]Jovanović, M. R. and Bamieh, B., "Componentwise energy amplification in channel flows," *Journal of Fluid Mechanics*, Vol. 534, 2005, pp. 145-183.

[29]Jeun, J., Nichols, J. W., and Jovanović, M. R., "Input-output analysis of high-speed axisymmetric isothermal jet noise," *Physics of Fluids*, Vol. 28, No. 4, 2016, pp. 1-20.